Microstructure Evolution of Commercial Pure Titanium During Interrupted In Situ Tensile Test

Qian Wang, Shiying Wang, Patrick Moll, Auriane Mandrelli, Jean-Sébastien Lecomte, Christophe Schuman

Microstructure evolution of commercial pure titanium during interrupted in-situ tensile test

Qian Wang [a,b], Shiying Wang [c], Patrick Moll [a,b], Auriane Mandrelli [a,b], Jean-Sébastien Lecomte [a,b,*], Christophe Schuman [a,b,**]

[a] Laboratoire d'Etude des Microstructures et de Mécanique des Matériaux (LEM3), Université de Lorraine, CNRS, Arts et Métiers ParisTech, Metz 57073, France

[b] Laboratory of Excellence on Design of Alloy Metals for low-mAss Structures (DAMAS), Université de Lorraine, Metz 57073, France

[c] School of Materials Science & Engineering, Changzhou University, Changzhou, Jiangsu 213164, China

***Corresponding author.**

****Corresponding author.**

E-mail adresses: jean-sebastien.lecomte@univ-lorraine.fr

christophe.schuman@univ-lorraine.fr

Abstract

Microstructure evolution of commercial pure titanium is investigated by interrupted in-situ electron backscatter diffraction (EBSD) measurement during tensile deformation along transverse direction at room temperature. After 24% elongation, the split basal texture of initial material is weakened and rotated around 90º along normal direction (**ND**). $\{11\bar{2}2\}$-$\{10\bar{1}2\}$ double twin is the main reason for the change of texture. The basal poles are rotated nearly perpendicular to **ND** by the primary $\{11\bar{2}2\}$ twin and back to **ND** through the reorientation of $\{10\bar{1}2\}$ secondary twin. Both Schmid factor criterion and displacement gradient accommodation are considered to predict the twin-induced texture evolution during **TD** tension. Kink bands formed by the accumulation of basal <*a*> dislocations are also observed in the deformed grain. The activation of other slip systems can deviate the rotation axis and reduce the rotation angle of kink boundary. Besides, the kink boundary with high basal dislocation density obviously hinder the twin transmission and simultaneously can be taken as a preferential nucleation site for $\{11\bar{2}2\}$ twin.

Keywords: Titanium; Tension; Texture; $\{11\bar{2}2\}$ twin; $\{10\bar{1}2\}$ twin; Kink band;

1. Introduction

Commercially pure titanium (CP-Ti) sheets have widely been used in chemical plants, consumer products, and heat exchangers [1,2], due to its high strength, corrosion resistance, burning resistance, and biological compatibility. Rolled α-Ti plate generally has a split-basal texture with the ***c***-axis of the hexagonal close-packed (HCP) lattice inclined at an angle of 20°–40° from the normal direction (**ND**) of the rolling plane towards the transverse direction (**TD**) [3]. Such a specific crystallographic feature introduces a severe anisotropy in deformation characteristics [4,5], mechanical properties [6] and formability [7], which is much more pronounced than that of other sheet metals such as steel and aluminum alloys. For this reason, understanding related mechanisms of deformation anisotropy in rolled α-Ti plate is an essential prerequisite.

The common plastic deformation modes in CP-Ti are slip (prismatic slip) and twinning ($\{10\bar{1}2\}$ extension and $\{11\bar{2}2\}$ contraction twinning). The ease of slip or twinning on a particular system is quantified by the critical resolved shear stress (CRSS). The relative activities of twinning and slip are also significantly dependent on the loading direction due to the strong rolling texture of as-received sample and the directional nature of deformation modes [8]. Dynamic compressive tests were carried out along **ND** in [9], maximum basal pole intensity was reoriented toward **ND** at the 40% thickness reduction. Apart from $\{11\bar{2}2\}$-$\{10\bar{1}2\}$ double twins, the accumulation of <*a*> and pyramidal <*c*+*a*> slips also gave rise to the strong basal texture. By conducting uniaxial compression along rolling direction (**RD**) and **ND**, Woo et al. [10] proposed that the primary and secondary twins are the main reason for the anisotropic texture evolution and Schmid factor (SF) criterion is a major mechanism controlling overall twinning characteristics. However, SF criterion is debatable for predicting general twin variant activation, the local stresses inside a grain could differ from the externally applied stress state, only 45%-50% of the cases are correct for the condition of rolling [11]. Displacement gradient accommodation (DGA) can more correctly predict the selection of secondary twin variants [12], and should also be considered on controlling the twin-induced texture evolution.

Compared with slip and twinning, “deformation kinking” is a less common deformation mode, but it is considered important for materials that exhibit strong plastic anisotropy, such as Zn [13,14], Mg/LPSO two-phase alloys [15,16], where LPSO phase is a long-period stacking ordered phase in Mg alloy. Hess and Barett [13] first proposed a dislocation-based model to explain kink band formation. In this model, cooperative operation followed by arrangement of basal dislocations to align perpendicular to the slip plane were believed to be the basic process

to form the deformation kink boundary. For HCP phase, the deformation kink band boundary was mainly constructed by the array of basal dislocations [14,17]. Besides, it is discovered recently that kink band is an effective deformation mode to accommodate the plastic strain in LPSO phase [18]. In LPSO phase, the kink band can be classified into three types according to Taylor axes of slips: $<1\bar{1}00>$ or $<0\bar{1}10>$ rotation type, $<0001>$ rotation type and $<1\bar{2}10>$ rotation type, which are produced by basal $<\boldsymbol{a}>$ slip, prismatic $<\boldsymbol{a}>$ slip and a combination of two basal slip variants, respectively. Furthermore, some researchers have argued that $\{11\bar{2}1\}$ twin can be regarded as "geometry-fixed deformation kink band" [19]. Jin et al. [17] proposed that $\{11\bar{2}1\}$ twin is formed by a gradual evolution from kink band through accumulative basal dislocation slips. However, the research on kinking deformation was rather limited in titanium alloys [17,20], because they undergo twinning as an accommodation mechanism against stress concentration.

In the present work, the microstructure of CP-Ti was observed by interrupted in-situ electron backscatter diffraction (EBSD) measurements during tensile tests at room temperature. The paper is structured as follows. Section 2 gives a description of the sample preparation for interrupted in-situ experiment and EBSD characterization. Section 3 presents the texture component after large deformation resulting from different twin modes and characters of the double twins and kink bands are introduced individually in detail. In section 4, the basal texture change induced by $\{11\bar{2}2\}$ - $\{10\bar{1}2\}$ double twin during **TD** tension is predicted by the combination of SF and DGA criterions.

2. Methodology

2.1 Experimental process

The material used in this work is rolled commercially pure titanium T40 (ASTM grade 2) sheet with the thickness of 1 mm. The sheet was annealed at 750 ^{o}C for 1 h to obtain a fully recrystallized microstructure. The tensile specimens were cut by electrical discharge wire-cutting and the gauge dimensions are shown in Fig. 1a. The loading direction was chosen to be parallel to **TD** of titanium plate. According to the work of Wronski et al. [21], a titanium T40 alloy plate was tested, the results showed that twins appeared frequently in the sample elongated along **TD** in contrast to the **RD** tensile sample.

The sample preparation and interrupted in-situ experiment generally followed the method of Wang et al. [22]. Sample surface was treated for orientation detection before loading, enough indexation rate (> 90%) can also be obtained with increased deformation amount. Interrupted

in-situ tension was performed step by step in the tensile machine MT100 as illustrated in Fig. 1b under the tensile speed of 150 μm/min. To follow the microstructure evolution of the same zone under EBSD measurement, the zone of interest at the center of tensile sample was marked by micro-indentation. After each step of tensile deformation, the sample was unloaded to calculate the engineering strain (respective 8%, 16%, and 24%) and then crystallographic characterization was performed.

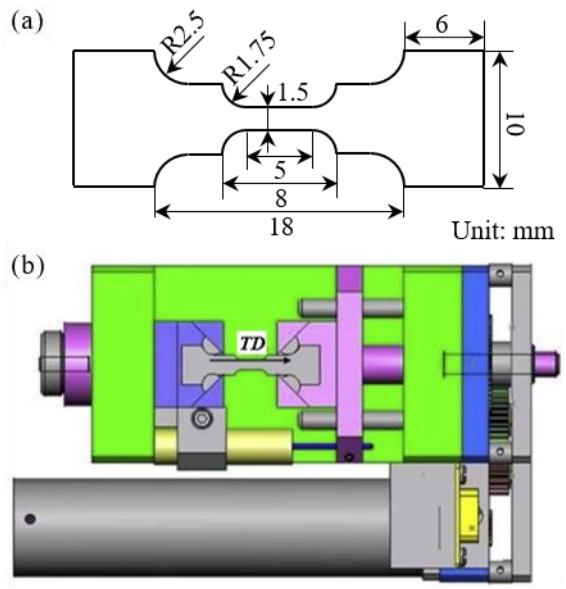

Fig. 1. (a) Tension sample dimension with thickness of 1 mm. (b) Sketch of the tension machine.

Before EBSD characterization, the sample was ground with SiC papers of grits from 1200# to 2400#, followed by electrolytic polishing using a solution of 10 vol% perchloric acid in methanol at 35 V and 5 ºC for 5 s. The characterization was performed using JSM 6490 scanning electron microscopy equipped with an EBSD camera with a specimen tilt of 70°, an accelerating voltage of 15 kV, a working distance of 15 mm and a step size of 1.5 μm. Four separate EBSD maps were obtained at the marked zone of the specimen to cover enough grains (around 84) and merged into one large image by Oxford-HKL channel 5 post-analysis software. Texture evolution was analyzed by ATEX software [23]. The geometrically necessary dislocation (GND) density was also calculated by ATEX software [23] according to the method described in literature [24].

2.2 Crystallography of twin and kink band

During deformation, the participation of twinning is required in titanium due to the limited slip systems. In the classical theory of deformation twinning, the parent lattice is reoriented by

atom displacements (***u***) which are equivalent to a simple shear of the lattice points. The twinning displacement in the twinning frame is shown in Fig. 2. The twinning frame is set up by: ***n*** // twinning shear direction, ***m*** // normal of twin habit plane and ***p*** // normal of shear plane. The displacement gradient tensor of twinning ($\mathbf{D}^{\mathbf{t}}$) has a simple form in the twinning frame [25]:

$$\mathbf{D}^{\mathbf{t}} = \frac{\partial u_i}{\partial Z_i} = \begin{bmatrix} 0 & 0 & s \\ 0 & 0 & 0 \\ 0 & 0 & 0 \end{bmatrix} \tag{1}$$

where ***u*** is displacement vector at position Z_i (i = 1…3) and s is the magnitude of twinning shear in Ti (c/a=1.587). The s values of $\{10\bar{1}2\}$ and $\{11\bar{2}2\}$ twins in titanium are 0.173 and 0.218, respectively. The orientation of the twin lattice can also be produced directly by a reflection of parent lattice in the twin habit plane or a 180° rotation about shear direction. Due to the crystal symmetry, the misorientations of $\{10\bar{1}2\}$ and $\{11\bar{2}2\}$ twins are 85°/<$11\bar{2}0$> and 64°/<$10\bar{1}0$>, respectively.

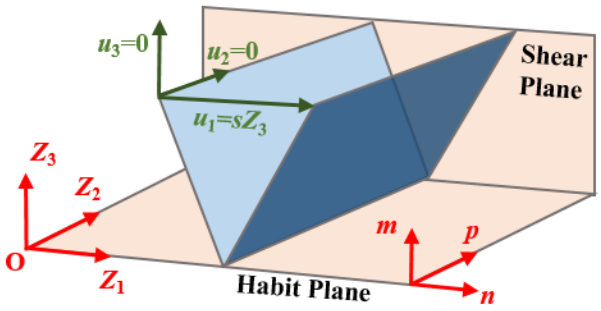

Fig. 2. Schematic diagram of twinning

The model for kinking mechanism in HCP crystal is firstly proposed by Hess and Barrett for a Zn single crystal [13], as shown in Fig. 3a. Kinking occurs by progressive lattice rotation within the band due to the accumulated basal slips perpendicular to slip plane as plastic deformation proceeds. It is different from twinning formed by abrupt shear into the final orientation, but it can be regarded as a origin of $\{11\bar{2}1\}$ twin nucleation [17]. To obtain a valuable geometric information, the lattice rotation axis and rotation angle $\Delta\phi$ were used to describe an individual kink band (Fig. 3b). The rotation axis can be determined through intragranular misorientation axis (IGMA) analysis [18,26] by matching the Taylor axis of a known slip mode. The Taylor axes of different slip systems in titanium are shown in Table 1. The kink band in HCP material is usually induced by basal slip [14,17], the misorientation axis is focus on <$10\bar{1}0$>. There appear three types of kink bands corresponding to three variants of basal slip, as shown in Table 2. The askew rotation axis from Taylor axis <$10\bar{1}0$> can be induced by the other slip

systems activated near the kink band. The rotation angle $\Delta\phi$ is between the basal plane of kink band and matrix, which is related to the dislocation density and the dislocation wall thickness [18]. The habit plane $\{1\bar{2}1k\}$ of each type kink band is rotated from $\{1\bar{2}10\}$ around $<10\bar{1}0>$ axis and the value k varies with the rotation angle $\Delta\phi$. The angle between $\{1\bar{2}10\}$ and $\{1\bar{2}1k\}$ is equals to the $\Delta\phi/2$.

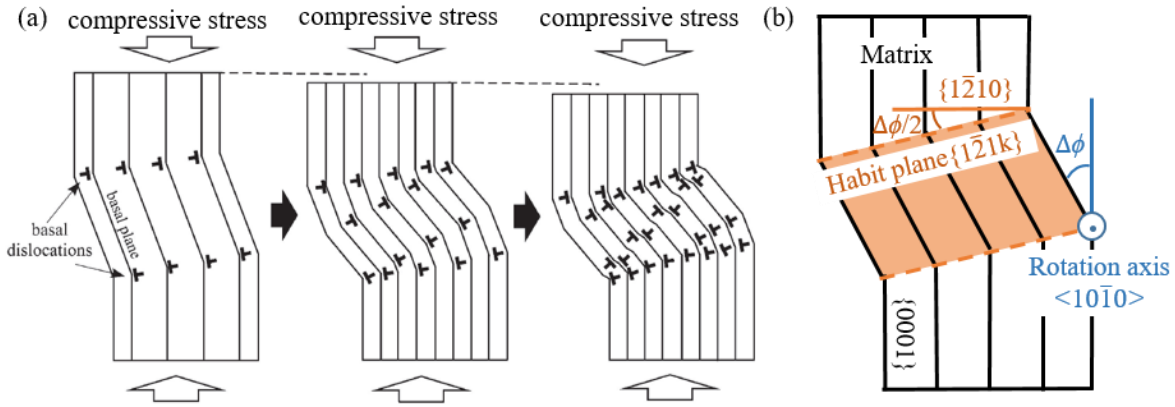

Fig. 3. (a) Model of deformation kink band formed in the Zn single crystal (reprinted from [13]). (b) Schematic on crystal rotation angle (misorientation angle) and crystal rotation axis of kink band.

3. Results

3.1 Twinning induced texture evolution

Fig. 4a-d show the microstructures of initial sample and the material stretched along **TD** to 8%, 16% and 24%, where **ND** axis was projected with the shown color bar. The as-received material has already fully recrystallized with the average grain size of around 100 μm. With the increase of elongation, there appear more and more twinning operations, which significantly change the grain oriantations.

Besides, the intragranular orientation change indicates the existence of GNDs after deformation. GNDs are created to accommodate the lattice curvature, the distribution of which can be measured with misorientation data from conventional Hough-based EBSD technique [24]. The Nye dislocation density tensor (α_{ij}) [24] is a sum over individual dislocation densities ρ^t of different dislocation types (t), each characterized by Burgers vector $\boldsymbol{b}^t$ and line vector $\boldsymbol{l}^t$,

$$\alpha_{ij}=\sum_{t=1}^{N} b_i^t l_j^t \rho^t \tag{2}$$

GND norm is the entrywise norm of the Nye Tensor [23],

$$\|\alpha\|=\sqrt{\alpha_{ij}\alpha_{ij}} \quad (3)$$

The average GND norms of initial and strained samples are measured by corresponding EBSD maps Fig. 4a-d. The results are presented in Fig. 5. Compared to the initial sample, the average GND norm is nearly unchanged after 8% strain and slightly increase in 16% tensile sample. The high GND density of 1.9×10^{-2} μm^{-1} after 24% tension shows that a huge amount of slip systems has been activated. Indeed, at large deformation, apart from twin, <*a*> and pyramidal <*c*+*a*> slips also gave rise to the texture evolution in pure titanium [9].

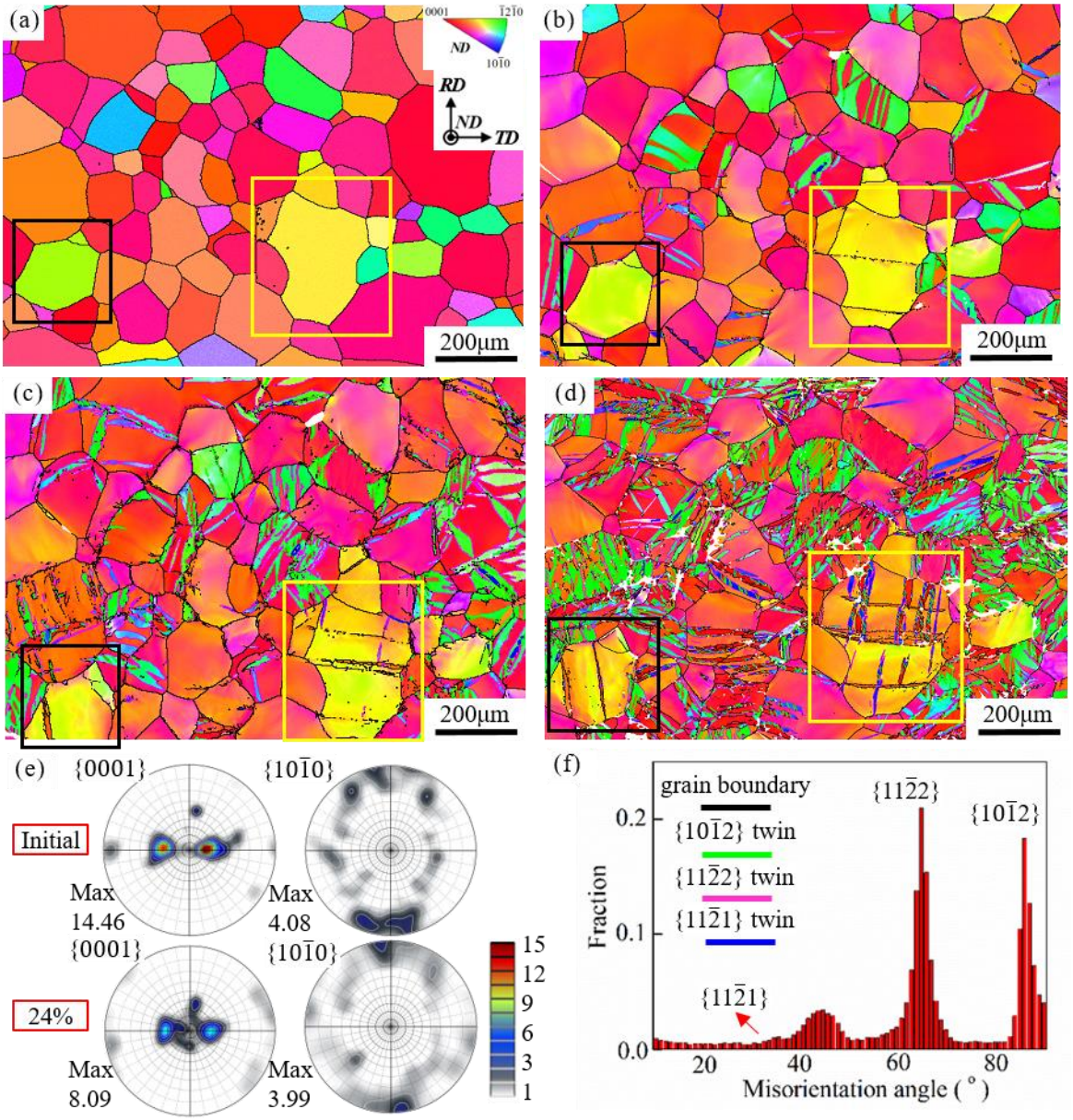

Fig. 4. Inverse pole figure (IPF) map of (a) initial microstructure (b) 8% (c) 16% (d) 24%. (e) Pole figures of {0001} and {10$\bar{1}$0} planes before and after 24% tension. (f) The corresponding misorientation angle distribution of 24% deformed sample.

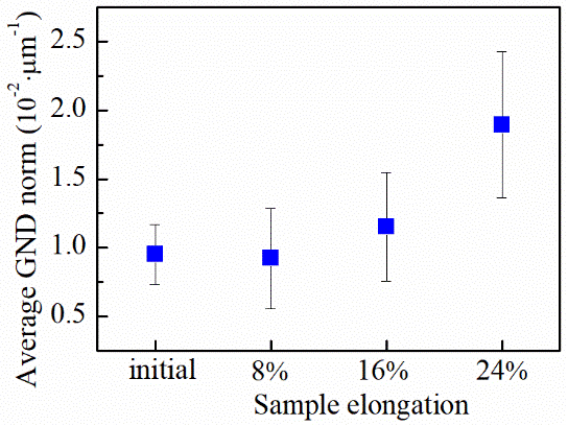

Fig. 5. The variation of average GND norms. Error bars are ± one standard deviation which incorporates multiple measurements in the same sample.

The texture evolution during tensile loading is illustrated in Fig. 4e. The initial material exhibits a typical split basal texture with *c*-axes inclined ± 30º from **ND** to **TD**. After 24% elongation, the initial split basal texture was weakened and partial *c*-axes trend to be rotated 90º around **ND**. Fig. 4f shows the histogram of misorientation distribution for the grain boundaries. Two significant peaks can be seen around 65º and 87º, which are attributed to the formation of $\{10\bar{1}2\}$ and $\{11\bar{2}2\}$ twin, respectively. Thus, the activation of $\{10\bar{1}2\}$ and $\{11\bar{2}2\}$ twin is the fundamental reason for the texture evolution during tensile test. $\{11\bar{2}1\}$ twin corresponds to the slight peak around 35º. A special peak between 40º and 50º arises from $\{11\bar{2}2\}$-$\{10\bar{1}2\}$ double twins, which has been investigated in-depth by Xu et al. [27]. The most frequent misorientation between the $\{10\bar{1}2\}$ secondary twin and titanium matrix is 48.44º around $<\bar{5}503>$, which is consistent with our experimental results.

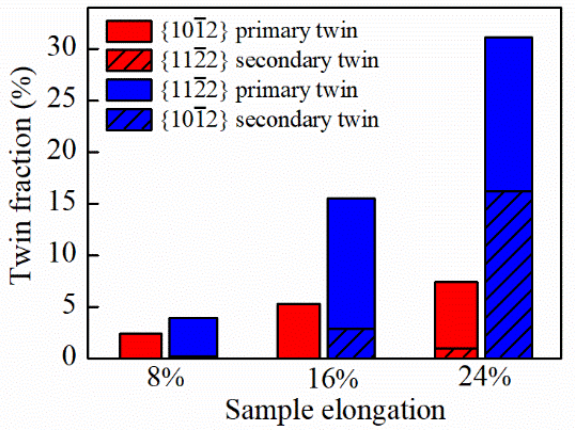

Fig. 6. Twin fraction in the sample with different elongations.

To calculate the twin area proportion, all the primary and secondary $\{10\bar{1}2\}$ and $\{11\bar{2}2\}$ twin grains formed in the observed 84 grains are manually picked out form the EBSD maps (Fig. 4b-d). The results are shown by bar chart in Fig. 6. For each strained sample, the area factions of primary $\{10\bar{1}2\}$ (red) and $\{11\bar{2}2\}$ (blue) twin are separately drawn with two bars, inside which the corresponding $\{11\bar{2}2\}$ and $\{10\bar{1}2\}$ secondary twin fraction are filled with diagonal stripes. In the 8% elongation sample, the fractions of $\{10\bar{1}2\}$ and $\{11\bar{2}2\}$ twin are low, respective 2.5% and 3.7%, and nearly no secondary twins are observed. After 16% tension, the fraction of $\{11\bar{2}2\}$ twin (blue) around 15.5% increases rapidly and is three times the $\{10\bar{1}2\}$ twin (5.3%). Besides, a small amount of $\{11\bar{2}2\}$-$\{10\bar{1}2\}$ double twins have been formed inside primary $\{11\bar{2}2\}$ twin grains. Compared with primary $\{11\bar{2}2\}$ twin, the increase of primary $\{10\bar{1}2\}$ twin fraction is relatively slight, indicating that **TD** tension is more favorable for $\{11\bar{2}2\}$ twin. Although the CRSS value of $\{11\bar{2}2\}$ twin is higher than $\{10\bar{1}2\}$ twin in CP-Ti at room temperature [28], the actual stimulation of twin system is governed by the combination of the SF and CRSS (i.e., activation stress = CRSS/SF). The $\{10\bar{1}2\}$ and $\{11\bar{2}2\}$ twin prefer to be activated when ***c***-axes are under tension and compression, respectively. Due to the basal texture of titanium sample (basal poles // **ND**), ***c***-axes are always compressed during **TD** tension and the formation of $\{10\bar{1}2\}$ twin is restrained. Thus, when tensile strain proceeds to 24%, the primary $\{10\bar{1}2\}$ twin fraction is almost unchanged and only a few secondary $\{11\bar{2}2\}$ twin occur. Noting that the primary $\{11\bar{2}2\}$ twin fraction (31.1%) is twice that of 16% elongation sample and half of the primary $\{11\bar{2}2\}$ twins are reoriented into secondary $\{10\bar{1}2\}$ twins to further accommodate the external tensile strain. Therefore, forming large amount of primary $\{11\bar{2}2\}$ and secondary $\{10\bar{1}2\}$ twins is the main reason for the texture change during **TD** tension.

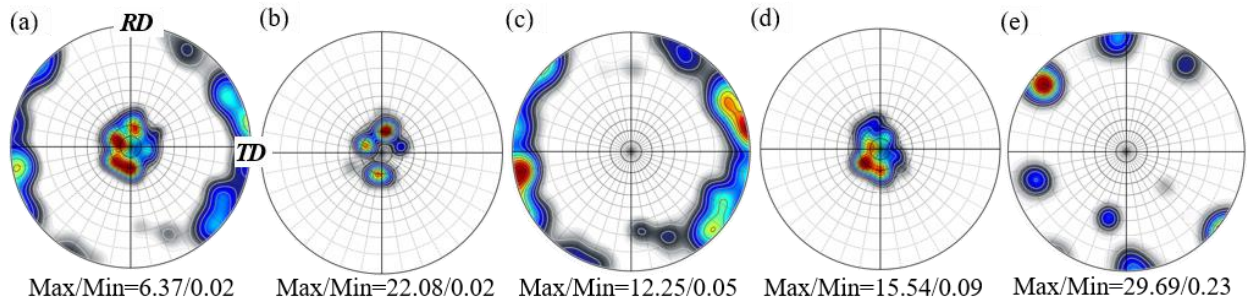

Fig. 7. {0001} pole figures of deformation twins (a) All the deformation twins. (b) Primary $\{10\bar{1}2\}$ twins. (c) Primary $\{11\bar{2}2\}$ twins. (d) Secondary $\{10\bar{1}2\}$ twins. (e) Secondary $\{11\bar{2}2\}$ twins.

The texture of twin formed in 24% elongation sample is calculated to investigate the specific orientation change induced by each type of twin during tensile deformation. The {0001} pole figures of different deformation twins are presented in Fig. 7. Fig. 7a shows the texture of all the deformation twins, the strong {0001} poles are focus along **ND**. There also appear some weak peaks around **TD**. These different peaks show the different effect of twins on texture evolution during deformation. According to the {0001} pole figure of each type twin (see Fig. 7b-e), the textures of primary and secondary $\{10\bar{1}2\}$ twin are similar focus on the center of pole figures and the textures of $\{11\bar{2}2\}$ twins are in **RD**-**TD** plane and close to **TD**. According to Fig. 6 the primary $\{11\bar{2}2\}$ and secondary $\{10\bar{1}2\}$ twins are dominant after 24% elongation. It can be derived that, under continuous tensile loading, the basal poles of as-received grains with basal texture are rotated into **RD**-**TD** plane by the formation of primary $\{11\bar{2}2\}$ twins, and then oriented back to **ND** after significant activation of secondary $\{10\bar{1}2\}$ twins.

The SF criterion is conveniently used as a reference for twin variant selection. It is based on the idealized hypothesis that the stress direction in individual grain is exactly the same as the nominal applied stress. Under uniaxial tension along **TD**,

$$SF = \cos(\theta)\cos(\lambda) \tag{4}$$

where θ is the angle between twinning plane normal and loading direction, and λ is the angle between shear direction and loading direction. Normalized Schmid factor (NSF) was calculated to compare the SF of activated twin variant with the other possible variants in the same grain [27].

$$NSF\ (i) = SF\ (i) / SF_{\max},\ i = 1\ldots6 \tag{5}$$

The maximum possible value of $NSF(i)$ is 1. In the present work, the NSFs of all the primary and secondary $\{10\bar{1}2\}$ and $\{11\bar{2}2\}$ twin in Fig. 4d (24% strain) are measured as shown in Fig. 8. The area faction of each twin mode is the same as the value in Fig. 6. The twin variants with actually high SFs are defined as $NSF \geq 0.9$ filled with diagonal stripes. For the primary $\{10\bar{1}2\}$ (red), secondary $\{11\bar{2}2\}$ (green), primary $\{11\bar{2}2\}$ (blue) and secondary $\{10\bar{1}2\}$ (pink) twin, the high SF twin fractions ($NSF \geq 0.9$) are respective 64.1%, 16.1%, 66.5% and 70.8%. The abnormally low fraction 16.1% is controversial due to that the activated secondary $\{11\bar{2}2\}$ twin is very few and insufficient for statistical analysis. The high SF twin fractions for the other three twin modes are relatively higher, showing that the variants with high SFs tend to be more active. According to Fig. 7, the oriented basal texture during tensile deformation is mainly depends on the primary $\{11\bar{2}2\}$ and secondary $\{10\bar{1}2\}$ twins, which always respects SF rule. The variant

selection induced by local strain accommodation and the prediction of tensile texture evolution will be further discussed in Section 4.

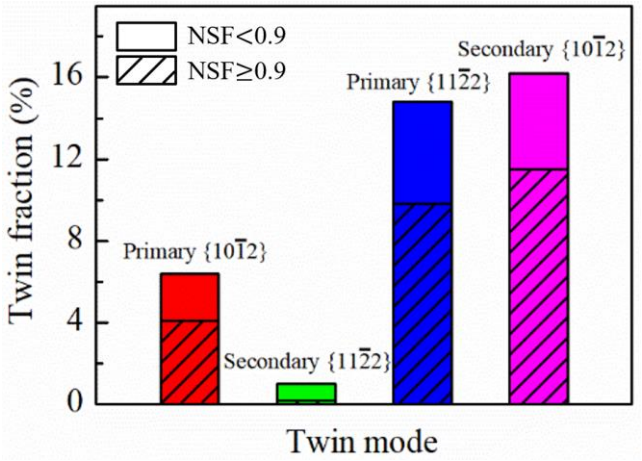

Fig. 8. Area fraction of twins as a function of the normalized Schmid factor

3.2 Double twin and grain boundary sliding

The interrupted in-situ microstructures of four typical grains are shown in Fig. 9. The orientations of G1 and G2 are favorable for primary {10$\bar{1}$2} tension and {11$\bar{2}$2} compression twin, respectively, followed by the formation of secondary {11$\bar{2}$2} and {10$\bar{1}$2} twin during continuous deformation. Six {10$\bar{1}$2} and {11$\bar{2}$2} twin variants are denoted by respective T_i and C_i (i = 1,2,3…6). In order to facilitate analysis, the twin variants of double twin are presented in the crystal frame of primary twin. Six twin variants of each twin system are given by their corresponding twin planes and shear directions, as shown in Table 3.

G1 has the orientation favorable for {11$\bar{2}$2} twin. Two primary {11$\bar{2}$2} twin variants are observed after 16% elongation, C_5 (SF: 0.42) and C_4 (SF: 0.15). In Fig. 9c and d, the size of C_4 variant with lower SF is larger than C_5. It is considered that variants achieving certain pertinent local strain accommodations in their neighborhoods can be preferentially activated [29]. Twins accommodated by the twins in neighboring grain have a great capacity to develop into large size [22]. Indeed, there appears adjoined twin to active large C_4 in the upside neighboring grain (G5), the accommodation mechanism can be found in discussion. After 24% elongation, secondary {10$\bar{1}$2} twins nearly cover the C_4 and C_5 twin. The formed double twins are C_4-T_5 and C_5-T_5. The variant selection of {11$\bar{2}$2} - {10$\bar{1}$2} double twin in CP-Ti under **ND** compression were explored in [30]. By the method of displacement gradient accommodation (DGA) criterion, they suggested that the C_i-T_i/T_{i+1} double twins are the most predominant

because the T_i/T_{i+1} variants have the highest capacity to accommodate the primary C_i twin. The other types of double twins are less. Indeed, the dominant double twin in G1 are C_4-T_5 and C_5-T_5. The variant selection of $\{11\bar{2}2\}$-$\{10\bar{1}2\}$ double twin between T_i and T_{i+1} will be further discussed in Section 4.

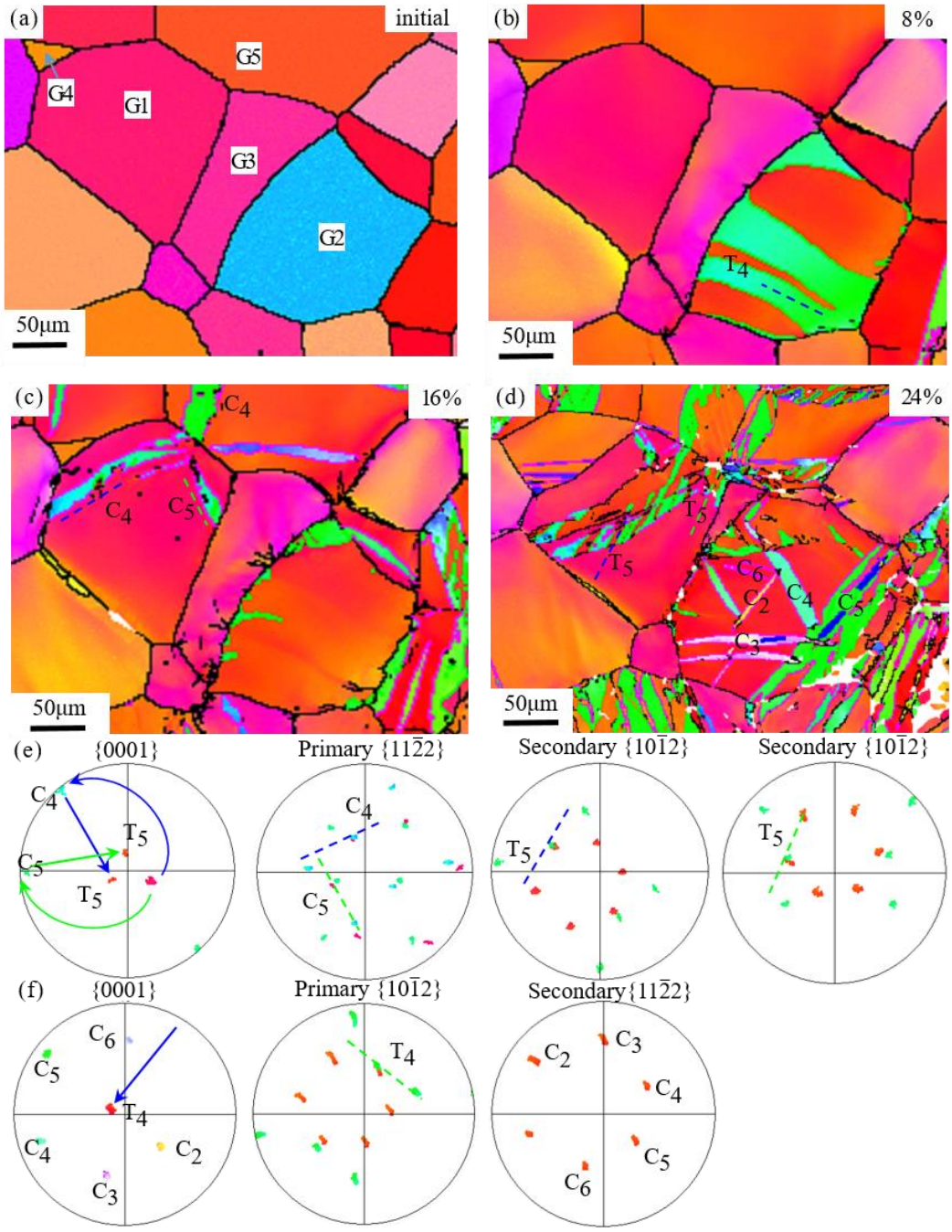

Fig. 9. The interrupted in-situ microstructures of four typical grains (G1-G4) during tension (a) initial (b) 8 %(c) 16 % (d) 24 %. (e) pole figures of $\{11\bar{2}2\}$-$\{10\bar{1}2\}$ double twins in G1 (f) pole figures of $\{10\bar{1}2\}$-$\{11\bar{2}2\}$ double twins in G2. The color of dots in pole figures is corresponding to IPF color. The dotted lines show the traces of primary and secondary twin planes. (Euler angles of G1: 75.7º, 28.6º, 24.9º; G2: 146.2º, 87.5º, 17.1º; G3: 97.0º, 142.5º, 36.0º and G4: 77.7º, 148.8º, 58.3º)

The orientation of G2 is favorable for the primary $\{10\bar{1}2\}$ twin. The $\{10\bar{1}2\}$ twin T_4 with largest SF (0.14) can be easily formed after a small elongation of 8% (see Fig. 9b). Different from the lenticular microscopy of primary $\{11\bar{2}2\}$ twin in G1, the primary $\{10\bar{1}2\}$ twin can quickly grow up and cover the whole grain after 16% elongation in Fig. 9c. The easy growth of $\{10\bar{1}2\}$ twin can be due to the lower twin shear than $\{11\bar{2}2\}$ twin. After 24% elongation, five secondary $\{11\bar{2}2\}$ variants are activated in T_4. There is not obvious variant selection for $\{10\bar{1}2\}$-$\{11\bar{2}2\}$ double twin in this work. The stimulation of these different secondary $\{11\bar{2}2\}$ twin variants is likely due to the complicated internal stress in primary $\{10\bar{1}2\}$ twin.

Furthermore, significant grain boundary sliding is observed in G3 and G4 during tensile deformation. With the increase of elongation, the accumulated heterogeneous deformation along grain boundaries produced by the accumulation of dislocations and/or twin shear, leads to orientation gradients exceeding 10° over 10–20 μm. At large strain, several slip systems, prism <*a*>, basal <*a*> and pyramidal <*c*+*a*> slips operate within grains and maintain strain compatibility requirements [9]. Grain boundary sliding can be induced by the accumulated dislocations to reduce the grain size of G3 and relax the local plastic anisotropy and deformation heterogeneities. As for G4, the orientation is favorable for $\{11\bar{2}2\}$ twin, but the grain size is small. It is well recognized that large grains facilitate the activity of deformation twin [31]. In the 24% strained sample, the twins in the fine grain with soft orientation are also stimulated to accommodate the larger external strain. And then, the grain boundaries expand outward to relax the twin shear and accelerate the twin growth, which finally leads to the increase of grain size of G4.

3.3 Kink band

Besides twinning and slip, deformation kinking also takes place in the tensile sample. The details of kink bands and their interactions with twin and slip are presented in Fig. 10 and Fig. 11. In Fig. 10a, two parallel kink bands are formed in G6 during deformation. According to Table 2 and the $<10\bar{1}0>$ pole figures in Fig. 10d and e, the rotation axis of the two kink bands is $[1\bar{1}00]$. Thus, they belong to K_1 variant and are denoted by K_{1L} (left) and K_{1R} (right). Their habit planes are respective $(11\bar{2}1)$ and $(\bar{1}\bar{1}2\ 0.5)$ as shown by the pole figures in Fig. 10d and e. According to the interrupted in-situ microstructures of G6 in Fig. 4a-d, in the black box at bottom left, K_{1L} is formed first at 16% strained sample, while K_{1R} is formed afterwards with further deformation. In Fig. 10a, K_{1L} is much thicker than K_{1R} indicating that the formed kink band can get thickened with increased deformation.

The average of the misorientation angle is measured by the values at randomly selected ten positions along kink band boundary. The average misorientation value for K_{1L} in 16% elongation sample is around 25.9º, which decrease to 12.5º after 24% elongation. Similarly, with the increase of strain, the average misorientation for K_{1R} around 27.2º will also decrease with further deformation. The reduced rotation angle of kink band means the decrease of basal dislocation density [18]. The IGMA distributions in Fig. 10b and c are drawn to show the different misorientation distributions of K_{1L} and K_{1R}. In 24% tensile sample, misorientation angles of K_{1R} are focused around <10$\bar{1}$0> axis, while the distribution of K_{1R} is discrete from <10$\bar{1}$0> axis to <0001> axis. <10$\bar{1}$0> and <0001> axis are Taylor axes of basal and prismatic <*a*> slip, respectively (Table 1). Therefore, the accumulated basal dislocations at kink band boundary can be transformed into prismatic dislocations or glide away during continuous deformation.

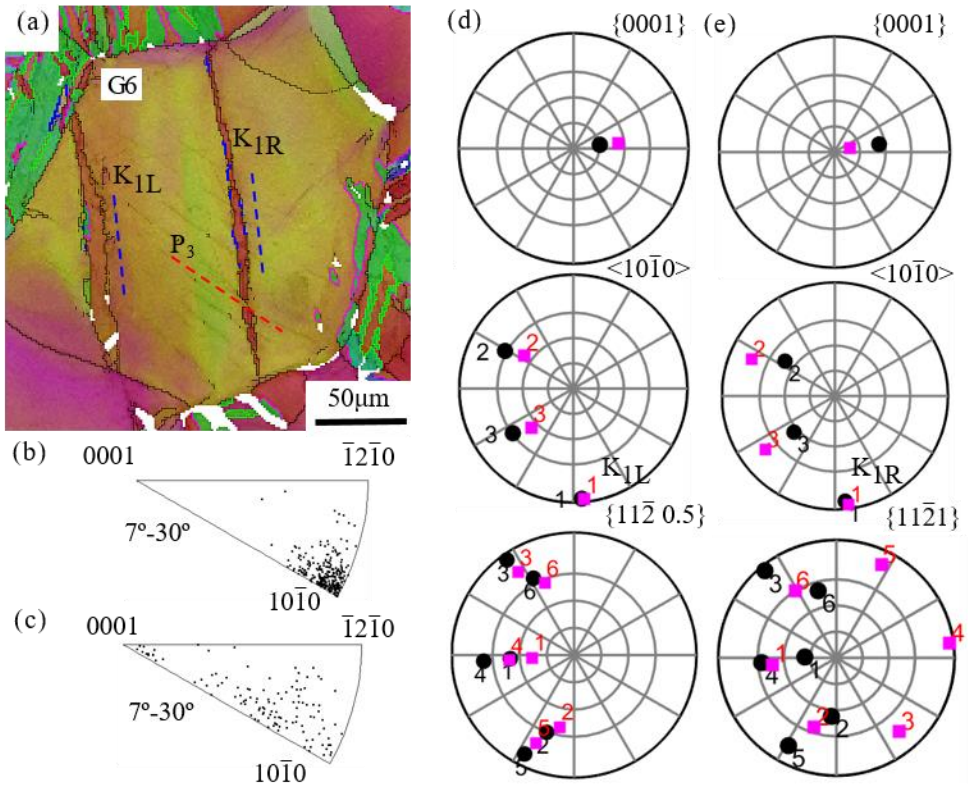

Fig. 10. (a) IPF map of G6 with kink band after 24% elongation. (b) and (c) IGMA distributions around kink band boundary of respective K_{1R} and K_{1L} obtained from misorientation angles of 7º-30º. (d) and (e) Pole figures of K_{1L} and K_{1R}, respectively. In pole figures, the pink and black dots represent the direction or plane in respective kink band and matrix. The dotted lines show the traces of kink band habit plane or slip plane. (Euler angle of matrix: 100.4º, 41.4º, 54.5º)

Noting that some segments of K_{1R} are identified as $\{11\bar{2}1\}$ twin boundary ($35^{o}/<10\bar{1}0>$). However, no $\{11\bar{2}1\}$ twin occur in K_{1L} showing that the twin segments can be formed at initial nucleation of kink band (K_{1R}) at 16% strain which are not stable in G6 and will disappear during further deformation. Jin et al. [17] proposed the formation mechanism of $\{11\bar{2}1\}$ twin through kinking in titanium. The $\{11\bar{2}1\}$ twin formed by kinking mechanism mainly occurs in the grains where only one basal slip is favorable and prismatic slips are suppressed. At the same time, the formed $\{11\bar{2}1\}$ twin has a quite high positive SF value. The SFs of the different plastic modes in G6 are presented in Table 4. According to Table 2, K_{1R} is formed by $(0001)[11\bar{2}0]$ dislocation (B_1). The high SF of B_1 (0.49) is favorable for the formation of kink band, while the activation of P_3 (Fig. 10a) with high SF (0.28) can locally rotate the $[1\bar{1}00]$ rotation axis of kink band and restrain the nucleation of $\{11\bar{2}1\}$ twin.

Fig. 11a present a grain (G7) with interaction of kink band with $\{11\bar{2}2\}$ twin. According to $\{11\bar{2}0\}$ pole figure in Fig. 11b, $\{11\bar{2}0\}$ plane trace is used to determine the kink band variant in G7, because the plane traces of habit planes $\{11\bar{2}k\}$ parallel to $\{11\bar{2}0\}$. All the four kink bands in G7 are K_2 variant with habit plane of $(1\bar{2}1k)$, formed by $(0001)[1\bar{2}10]$ (B_2) basal dislocations. The two close kink bands in the middle of G7 are thicker than the other two on the upper and lower sides likely due to the earlier nucleation and different local stress. Similarly to G6, the nucleation of $\{11\bar{2}1\}$ twin from K_2 is restrained after large deformation due to the high activity of prismatic slips, both P_1 and P_3 are observed in Fig. 11a. Specially, the kink bands always connect with triple junction of grain boundaries. It can be therefore speculated that stress concentration at triple junction play a favorable role on the kink band nucleation. In addition, the SF of B_2 is extremely low (0.01) in Table 4, while the SFs of prismatic slips are high, P_1 (0.39) and P_3 (0.45). Different from G7, the SF of B_1 (0.49) in G6 is high and P_3 SF (0.28) is relatively lower. The kinking deformation can be stimulated in G6 and G7 with different active slip systems, thus the critical stress conditions for kink band nucleation need to be further investigated.

Furthermore, in the yellow boxes of Fig. 4a-d, the microstructure evolution of G7 is presented. With increased strain, $\{11\bar{2}2\}$ twin nucleation occurs at 16% strain and interacts with pre-existing kink bands. The basal dislocation on the kink boundary in Fig. 11a corresponds to perfect <*a*> edge dislocation and the mixed dislocations with same Burgers vector is localized around kink boundary [15]. The growth of C_1 is hindered by the parallel kink bands with complicated dislocations in G7, which shows the work hardening mechanism produced by the formation of kink bands. According to Table 4, C_1 is the most favorable twin with highest SF

(0.40), while C_2 stimulated at the kink band boundary has negative SF (-0.01). The negative SF C_2 cannot accommodate external stress, that is induced by the accumulated dislocation and stress concentration around kink band.

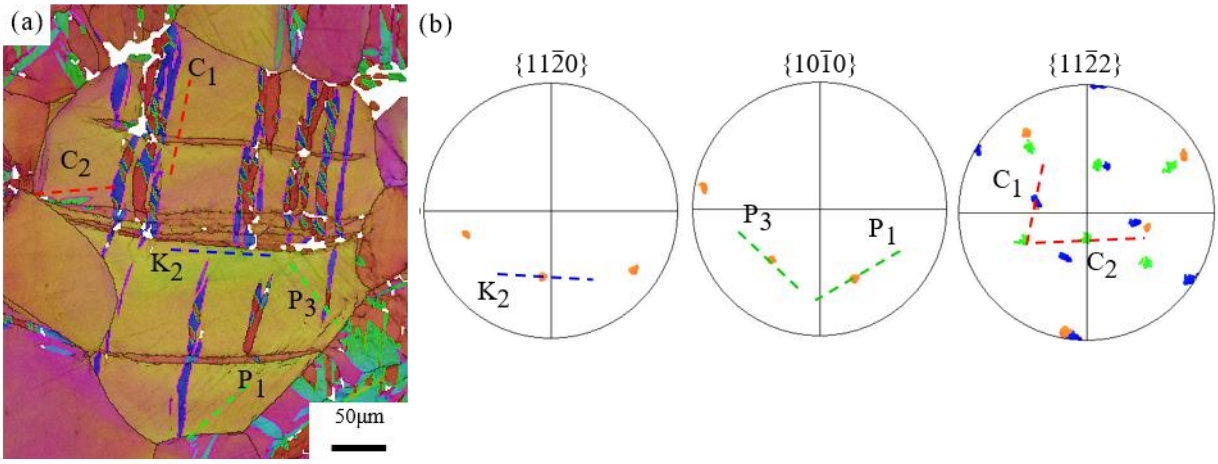

Fig. 11. (a) IPF map of G7 after 24% elongation. (b) {11$\bar{2}$0}, {10$\bar{1}$0} and {11$\bar{2}$2} pole figures. The color of dots in pole figures correspond to IPF color. The dotted lines show the traces of kink band habit plane, slip and twin plane. (Euler angle of matrix: 165.0º, 37.4º, 8.7º)

4. Discussion

According to the results in Section 3.1, texture evolution during tension is mainly controlled by primary {11$\bar{2}$2} and secondary {10$\bar{1}$2} twins. The variant selection of {11$\bar{2}$2}-{10$\bar{1}$2} double twins in G1 (Fig. 9) is studied as an example. First, the accommodation of primary {11$\bar{2}$2} twins C_5 (SF: 0.42) and C_4 (SF: 0.15) by neighboring grain is investigated by transforming the displacement gradient tensor of twinning into the crystal frame of neighboring grain [29]. The method of twinning and crystal coordinate transformation is shown in Appendix. $\mathbf{D}_{g3}^{c5}$ refers to the displacement gradient tensors of C_5 transformed from the twin frame into G3 crystal frame and $\mathbf{D}_{g5}^{c4}$ is the displacement gradient tensors of C_4 transformed from the twin frame into G5 crystal frame, as shown in Table 5. The crystal frame of α-Ti is ***x***//[10$\bar{1}$0], ***y***//[$\bar{1}$2$\bar{1}$0] and ***z***//[0001]. D_{xz} and D_{yz} represent the strain can be accommodated by single and double basal slips, D_{xy} and D_{xy} indicate the accommodation by single and double prismatic slip, the D_{zx} and D_{zy} are the accommodation by twinning.

According to $\mathbf{D}_{g3}^{c5}$, the large values of D_{xz} (0.11) and D_{yz} (0.18) show that only basal slips in G3 can accommodate the C_5 twin in G1. The basal slip is difficult slip system than prismatic slip in titanium and not enough to accommodate the shear for twin growth, and thus the size of

C_5 twin is limited. As for C_4, it can be accommodated by twinning in the upper grain because of the large D_{zx} (-0.13) of $\mathbf{D}^{c4}_{g5}$. Indeed, obvious twin interaction between them can be observed in Fig. 7c and the interaction is more significant in Fig. 9d. The $\mathbf{D}^{c4}_{g5}$ is transformed into the twinning frame of activated $\{11\bar{2}2\}$ twin (C_4) in G5 ($\mathbf{D}^{c4}_{c1}$) using the method in Appendix. The resulting tensor $\mathbf{D}^{c4}_{c1}$ is shown in Table 5 and has a large positive D_{13} (0.19), which means the twin in G5 can accommodate the shear of C_4. Thus, the twin with lower SF can be more stable when it can be accommodated by the twin in the neighbor grain. However, the volume fraction of twin variants showing such a non-Schmid behavior is limited in the whole sample, the SF criterion is a major mechanism controlling twinning [10].

C_4-T_5 is the dominant double twin in G1. Indeed, the formed $\{11\bar{2}2\}$-$\{10\bar{1}2\}$ double twins in α-Ti always follow the C_i-T_i/T_{i+1} group proposed by Xu et al. [30]. The T_i/T_{i+1} variants are activated to accommodate the local shear of primary C_i twin. To further investigate the variant selection between T_i and T_{i+1} variant, the accommodation capacity on C_i twinning is compared by transforming the $\mathbf{D}^{t}$ of all the C_4, T_4 and T_5 into the crystal frame of C_4. The results are shown in Table 5. Compared with $\mathbf{D}^{t4}_{g(c4)}$, all the nine components of $\mathbf{D}^{t5}_{g(c4)}$ tensor are non-zero and the same sign with $\mathbf{D}^{c4}_{g(c4)}$. It means that T_5 can more effectively accommodate the local strain of C_4 along all the crystal directions than T_4. To verify the above result, all the double twins in Fig. 4d are determined, 64.4% (area fraction) of secondary $\{10\bar{1}2\}$ twins belongs to the group C_i-T_{i+1}, which is a little smaller than the twin fraction respecting the SF rule, 70.8% twin with NSF ≥ 0.9 (Fig. 8). According to Fig. 7c, the basal poles of primary $\{11\bar{2}2\}$ twins oriented along **TD** after 24% tension, thus the NSF values of six secondary $\{10\bar{1}2\}$ variants are always similar and larger than 0.9. However, C_i-T_{i+1} group can more efficiently determine the most favorable variant T_{i+1}.

According to the above analysis, to predict the texture evolution induced by $\{11\bar{2}2\}$-$\{10\bar{1}2\}$ double twins, the activation of primary $\{11\bar{2}2\}$ twin is determined by SF criterion and the selected secondary $\{10\bar{1}2\}$ twin follows C_i-T_{i+1}. The {0001} pole figure of initial sample in Fig. 4e shows the split basal texture with *c*-axis oriented from **ND** to **TD** and the ***a***-axis is random. The Euler angles of initial grain orientations are set as [90º, 30º, 0-10º & 50-60º] (right basal poles) and [270º, 30º, 180-190 º & 230-240º] (left basal poles). The initial orientations of [90º, 30º, 10-50º] and [270º, 30º, 190-230º] with the SFs of primary $\{11\bar{2}2\}$ twins less than 0.4 are excluded. The basal pole locations of selected primary $\{11\bar{2}2\}$ and secondary $\{10\bar{1}2\}$ twins are calculated and projected into pole figure (see Fig. 12). The basal poles of primary $\{11\bar{2}2\}$ twins

(blue) are less than 10º oriented from **TD** and the basal poles of secondary $\{10\bar{1}2\}$ twins (red) are oriented around 20º from **ND** to **RD**. The prediction is consistent to the Fig. 7a. The weak peak at C_4 position (Fig. 7c) and strong peak at T_5 position (Fig. 7d) shows the main double twin in the observed area of 24% elongation sample is C_4-T_5.

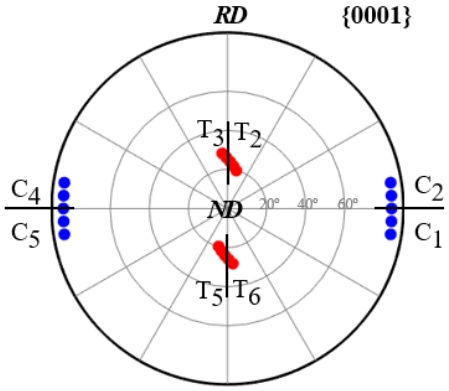

Fig. 12. The basal pole location of primary $\{11\bar{2}2\}$ twin (C_i) with SF>0.4 and corresponding secondary $\{10\bar{1}2\}$ twin (T_{i+1})

5. Conclusion

In this work, interrupted in-situ tension was performed to investigate the microstructure evolution of commercial pure titanium during plastic deformation.

$\{11\bar{2}2\}$ compression and $\{10\bar{1}2\}$ tension twins are dominant twin modes on the observed surface after 8%, 16% and 24% elongation along **TD**. The anisotropic activation of deformation twin, especially $\{11\bar{2}2\}$-$\{10\bar{1}2\}$ double twin, is the reason for the texture evolution during deformation. The primary $\{11\bar{2}2\}$ twin is responsible for the aligned basal poles along **TD** and the secondary $\{10\bar{1}2\}$ twin reoriented the basal poles parallel to **ND**. Although some non-Schmid twins are induced by local stress concentration, more than 60% deformation twins respect SF criterion. To predict the texture evolution produced by $\{11\bar{2}2\}$-$\{10\bar{1}2\}$ double twin, the primary $\{11\bar{2}2\}$ variant followed SF rule and the variant selection of secondary $\{10\bar{1}2\}$ twin was determined by DGA.

Interestingly, kink bands formed by the accumulation of basal <*a*> dislocations were observed. The kink band variant were determined by the trace of habit plane $\{11\bar{2}k\}$. The activation of other slip systems, for example prismatic <*a*> slips, can deviate the rotation axis and reduce the rotation angle of kink boundary. Besides, twin growth extremely hindered by kink boundary is responsible for the hardening behavior of CP-Ti at large strain.

Acknowledgements

The first author Qian Wang is grateful to the China Scholarship Council for the support of her Ph.D. study in France.

References

1 M. Ishiki, T. Kuwabara, and Y. Hayashida: *Int. J. Mater. Form.*, 2011, vol. 4, pp. 193–204.
2 Z. Zeng, Y. Zhang, and S. Jonsson: *Mater. Des.*, 2009, vol. 30, pp. 3105–11.
3 Y.B. Chun, S.H. Yu, S.L. Semiatin, and S.K. Hwang: *Mater. Sci. Eng. A*, 2005, vol. 398, pp. 209–19.
4 N.P. Gurao, R. Kapoor, and S. Suwas: *Acta Mater.*, 2011, vol. 59, pp. 3431–46.
5 M. Battaini, E. V Pereloma, and C.H.J. Davies: *Metall. Mater. Trans. A*, 2007, vol. 38, pp. 276–85.
6 S. Panda, S.K. Sahoo, A. Dash, M. Bagwan, G. Kumar, S.C. Mishra, and S. Suwas: *Mater. Charact.*, 2014, vol. 98, pp. 93–101.
7 X. Huang, K. Suzuki, and Y. Chino: *Scr. Mater.*, 2010, vol. 63, pp. 473–6.
8 M.H. Yoo: *Metall. Trans. A*, 1981, vol. 12, pp. 409–18.
9 Y. Ren, X. Zhang, T. Xia, Q. Sun, and Q. Liu: *Mater. Des.*, 2017, vol. 126, pp. 123–34.
10 J.W. Won, D. Kim, S.G. Hong, and C.S. Lee: *J. Alloys Compd.*, 2016, vol. 683, pp. 92–9.
11 S. Wang, C. Schuman, L. Bao, J.S. Lecomte, Y. Zhang, J.M. Raulot, M.J. Philippe, X. Zhao, and C. Esling: *Acta Mater.*, 2012, vol. 60, pp. 3912–9.
12 S. Xu, M. Gong, Y. Jiang, C. Schuman, J.S. Lecomte, and J. Wang: *Acta Mater.*, 2018, vol. 152, pp. 58–76.
13 J.B. Hess and C.S. Barrett: *JOM*, 1949, vol. 1, pp. 599–606.
14 K. Hagihara, T. Mayama, M. Honnami, M. Yamasaki, H. Izuno, T. Okamoto, T. Ohashi, T. Nakano, and Y. Kawamura: *Int. J. Plast.*, 2016, vol. 77, pp. 174–91.
15 T. Matsumoto, M. Yamasaki, K. Hagihara, and Y. Kawamura: *Acta Mater.*, 2018, vol. 151, pp. 112–24.
16 S. Yamasaki, T. Tokuzumi, W. Li, M. Mitsuhara, K. Hagihara, T. Fujii, and H. Nakashima: *Acta Mater.*
17 S. Jin, K. Marthinsen, and Y. Li: *Acta Mater.*, 2016, vol. 120, pp. 403–14.
18 M. Yamasaki, K. Hagihara, S.I. Inoue, J.P. Hadorn, and Y. Kawamura: *Acta Mater.*, 2013, vol. 61, pp. 2065–76.
19 N.J. Lane, S.I. Simak, A.S. Mikhaylushkin, I.A. Abrikosov, L. Hultman, and M.W. Barsoum: *Phys. Rev. B*, 2011, vol. 84, p. 184101.
20 Y. Zheng, W. Zeng, Y. Wang, and S. Zhang: *Mater. Sci. Eng. A*, 2017, vol. 702, pp. 218–24.
21 S. Wronski, M. Jedrychowski, J. Tarasiuk, and B. Bacroix: *Mater. Sci. Eng. A*, 2017, vol. 692, pp. 113–26.
22 S. Wang, Y. Zhang, C. Schuman, J.S. Lecomte, X. Zhao, L. Zuo, M.J. Philippe, and C. Esling: *Acta Mater.*, 2015, vol. 82, pp. 424–36.
23 B. Beausir and J.-J. Fundenberger: *Analysis Tools for Electron and X-Ray Diffraction, ATEX - Software, Université de Lorraine - Metz*, 2017.
24 W. Pantleon: *Scr. Mater.*, 2008, vol. 58, pp. 994–7.
25 É. Martin, L. Capolungo, L. Jiang, and J.J. Jonas: *Acta Mater.*, 2010, vol. 58, pp. 3970–83.
26 Y.B. Chun, M. Battaini, C.H.J. Davies, and S.K. Hwang: *Metall. Mater. Trans. A*, 2010, vol. 41, pp. 3473–87.
27 S. Xu, L.S. Toth, C. Schuman, J.-S. Lecomte, and M.R. Barnett: *Acta Mater.*, 2017, vol. 124, pp. 59–70.
28 T. Hama, A. Kobuki, and H. Takuda: *Int. J. Plast.*, 2017, vol. 91, pp. 77–108.
29 J.J. Jonas, S. Mu, T. Al-Samman, G. Gottstein, L. Jiang, and Ė. Martin: *Acta Mater.*, 2011, vol. 59, pp. 2046–56.
30 S. Xu, M. Gong, C. Schuman, J.-S. Lecomte, X. Xie, and J. Wang: *Acta Mater.*, 2017, vol. 132, pp. 57–68.
31 A. Ghaderi and M.R. Barnett: *Acta Mater.*, 2011, vol. 59, pp. 7824–39.

Appendix

To investigate the accommodation mechanism, the displacement gradient tensor of twinning $\mathbf{D^t}$ is always transformed into other coordinate system, such as crystal system, sample system or another twinning system. First, we need to build the coordinate rotation matrix from twinning system to crystal system.

$$\mathbf{R_{tg}} = \begin{bmatrix} n_1 & n_2 & n_3 \\ p_1 & p_2 & p_3 \\ m_1 & m_2 & m_3 \end{bmatrix} \quad \text{(A1)}$$

where $\boldsymbol{n}$, $\boldsymbol{m}$ and $\boldsymbol{p}$ represent the twinning shear direction ($\boldsymbol{n}$), normal of twin habit plane ($\boldsymbol{m}$) and normal of shear plane ($\boldsymbol{p}$). The coordinate rotation matrix sample system to crystal system is:

$$\mathbf{R_{gs}} = \mathbf{R}_{\varphi_2} \cdot \mathbf{R}_{\Phi} \cdot \mathbf{R}_{\varphi_1}$$

$$\mathbf{R}_{\varphi_1} = \begin{bmatrix} \cos\varphi_1 & \sin\varphi_1 & 0 \\ -\sin\varphi_1 & \cos\varphi_1 & 0 \\ 0 & 0 & 1 \end{bmatrix} \quad \text{(A2)}$$

$$\mathbf{R}_{\Phi} = \begin{bmatrix} 1 & 0 & 0 \\ 0 & \cos\Phi & \sin\Phi \\ 0 & -\sin\Phi & \cos\Phi \end{bmatrix} \quad \text{(A3)}$$

$$\mathbf{R}_{\varphi_2} = \begin{bmatrix} \cos\varphi_2 & \sin\varphi_2 & 0 \\ -\sin\varphi_2 & \cos\varphi_2 & 0 \\ 0 & 0 & 1 \end{bmatrix} \quad \text{(A4)}$$

where φ_1, Φ and φ_2 are Euler angles from HKL system. The displacement gradient tensor of Twin 1 ($\mathbf{D^{t1}}$) is transformed from Twin 1 frame ($\mathbf{D^{t1}_{t1}}$) to crystal frame of Grain 1 ($\mathbf{D^{t1}_{g1}}$) as follows:

$$\mathbf{D^{t1}_{g1}} = \mathbf{R^{-1}_{t1g1}} \cdot \mathbf{D^{t1}_{t1}} \cdot \mathbf{R_{t1g1}} \quad \text{(A5)}$$

The transformation of $\mathbf{D^{t1}}$ from Grain 1 frame ($\mathbf{D^{t1}_{g1}}$) to sample frame ($\mathbf{D^{t1}_{s}}$) to Grain 2 frame ($\mathbf{D^{t1}_{g2}}$) is:

$$\mathbf{D^{t1}_{g2}} = \mathbf{R_{g2s}} \cdot \mathbf{D^{t1}_{s}} \cdot \mathbf{R^{-1}_{g2s}} = \mathbf{R_{g2s}} \cdot \mathbf{R^{-1}_{g1s}} \cdot \mathbf{D^{t1}_{g1}} \cdot \mathbf{R_{g1s}} \cdot \mathbf{R^{-1}_{g2s}} \quad \text{(A6)}$$

The transformation of $\mathbf{D^{t1}}$ from Grain 2 frame ($\mathbf{D^{t1}_{g2}}$) to the frame ($\mathbf{D^{t1}_{t2}}$) of Twin 2in Grain 2 is:

$$\mathbf{D^{t1}_{t2}} = \mathbf{R_{t2g2}} \cdot \mathbf{D^{t1}_{g2}} \cdot \mathbf{R^{-1}_{t2g2}} \quad \text{(A7)}$$